

2015-01-01

# Microscopic and Spectroscopic Analysis of Cadmium Telluride

Jessica Goretty Salazar

University of Texas at El Paso, JGSalazar@miners.utep.edu

Follow this and additional works at: [https://digitalcommons.utep.edu/open\\_etd](https://digitalcommons.utep.edu/open_etd)



Part of the [Physics Commons](#)

---

## Recommended Citation

Salazar, Jessica Goretty, "Microscopic and Spectroscopic Analysis of Cadmium Telluride" (2015). *Open Access Theses & Dissertations*. 1149.

[https://digitalcommons.utep.edu/open\\_etd/1149](https://digitalcommons.utep.edu/open_etd/1149)

This is brought to you for free and open access by DigitalCommons@UTEP. It has been accepted for inclusion in Open Access Theses & Dissertations by an authorized administrator of DigitalCommons@UTEP. For more information, please contact [lweber@utep.edu](mailto:lweber@utep.edu).

# MICROSCOPIC AND SPECTROSCOPIC ANALYSIS OF CADMIUM TELLURIDE

JESSICA G. SALAZAR

Department of Physics

APPROVED:

---

Felicia S. Manciu, Ph.D., Chair

---

Marian Manciu, Ph.D.

---

Stella Quinones, Ph.D.

---

Cristian Botez, Ph.D.

---

Charles H. Ambler, Ph.D.  
Dean of the Graduate School

Copyright

by

Jessica G Salazar

2015

MICROSCOPIC AND SPECTROSCOPIC ANALYSIS OF CADMIUM TELLURIDE

by

JESSICA G. SALAZAR, B.S.

THESIS

Presented to the Faculty of the Graduate School of

The University of Texas at El Paso

in Partial Fulfillment

of the Requirements

for the Degree of

Master of Science

Department of Physics

THE UNIVERSITY OF TEXAS AT EL PASO

May 2015

## Abstract

Cadmium telluride (CdTe) remains one of the materials of interest in the fabrication of photovoltaic cells and infrared devices, mainly because of its suitable crystal structure as well as of its small, direct bandgap of 1.5 eV. Since development of such devices requires a high quality and low defect material, the goal of this study is to microscopically and spectroscopically examine not only crystallinity, but also the induced stress in the material due to the effect of substrate orientation. This information is valuable if optimization of sample growth conditions is envisioned. Prior to CdTe deposition by close-spaced sublimation (CSS), Si (111) and (211) substrates were patterned using photolithography and dry etching to create 500 nm to 1  $\mu$ m pillars. Scanning electron microscopy (SEM) images besides demonstrating uniform, selective growth of polycrystalline CdTe, reveal fewer defects and less twin-microcrystallite formation if Si (211) is used. Crystallinity of the samples was investigated by Fourier transform infrared absorption and Raman spectroscopies. The far-infrared transmission data show the presence of transverse optical (TO) and surface optical (SO) modes, the latter being direct evidence of confinement in such a material. Qualitative identification of the induced stress in the samples was achieved by performing confocal Raman mapping microscopy on their surfaces. These investigations indicate that the deposited material is under compressive stress, largely because of the high lattice mismatch between CdTe and the Si substrate. As high quality materials with excellent ordered structure are needed for developing photovoltaic devices, the results of this research demonstrate the importance of detailed, comprehensive analysis in optimizing and improving CdTe characteristics.

## Table of Contents

Abstract .....	iv
Table of Contents .....	v
Table of Figures .....	vii
Chapter 1: Background .....	1
1.1 Introduction to semiconductors .....	1
1.2 Solar Cells .....	2
1.2.1 Anatomy of a solar cell .....	2
1.2.2 Cadmium telluride for future use in photovoltaics .....	4
1.3 Infrared detectors.....	5
1.3.1 Cadmium telluride for use in infrared detectors .....	6
1.3 Dosimetry .....	8
1.3.1 Basics of radiation detectors .....	8
1.3.2 Properties needed for radiation detection.....	9
1.3.3 Cadmium telluride for radiation detectors.....	10
1.4 Digital radiography .....	11
1.4.1 X-rays .....	12
1.4.2 Computed Tomography.....	12
1.5 Cardiac function monitoring.....	13
1.5.1 Current gamma cameras .....	13
1.5.2 Cadmium telluride for use in gamma cameras.....	14
1.6 Concluding remarks .....	14
1.7 Limitations of widespread use of cadmium telluride .....	15
1.7.1 Cadmium toxicity .....	16
1.7.2 Limited supply of tellurium.....	16
1.7.3 Recycling of solar cells .....	17
Chapter 2: Methodology .....	18
2.1 Introduction to Spectroscopic Techniques .....	18
2.2 Raman Spectroscopy .....	19
2.2.1 Classical Wave Representation of Raman Scattering .....	19
2.2.2 Quantum Particle Representation of Raman Scattering .....	21
2.2.3 Experimental Set Up .....	23
2.3 Fourier Transform Infrared Spectroscopy .....	24
2.3.1 The Michelson Interferometer and Interpretation of Data .....	25
2.3.2 Experimental Set up .....	28
2.4 Comparison of Raman and FTIR .....	30
2.5 Sample Preparation .....	31

Chapter 3: Results and discussion .....	34
3.1 Introduction to characterization of cadmium telluride .....	34
3.2 SEM and Raman analysis of sample grown on Si(111) .....	35
3.3 Raman analysis of sample grown on Si(211) .....	38
3.4 FTIR spectroscopy results .....	39
Chapter 4: Conclusions .....	43
References .....	45
Curriculum vita .....	49

## Table of Figures

Figure 1-1.....	3
Figure 2-1.....	22
Figure 2-2.....	24
Figure 2-3.....	25
Figure 2-4.....	27
Figure 2-5.....	28
Figure 2-6.....	29
Figure 3-1.....	35
Figure 3-2.....	35
Figure 3-3.....	37
Figure 3-4a-b.....	38
Figure 3-5a-c.....	40



## Chapter 1: Background

### 1.1 Introduction to semiconductors

In 1833 Michael Faraday discovered that the electrical conductivity in silver sulfide, or as he called it “sulphurette of silver,” increased with increasing temperature. This is notable behavior because it is unlike the decreasing electrical conductivity of metals with increasing temperature. Thus came the first recorded observation of semiconductor behavior. Faraday theorized that raising the temperatures leads to an increase in the density of charge carriers hence increasing the conductivity of the material. Six years later in 1839, Edmond Becquerel discovered the photovoltaic effect by observing the voltage of a solid and a liquid when struck by light. Becquerel discovered that a current was generated when silver chloride placed in an acidic solution was illuminated. In 1956, William Shockley, John Bardeen, and Walter Brattain were awarded the Nobel Prize in Physics for their work on semiconductors the discovery of the transistor effect. Semiconductors have come to be responsible for dramatic advances in science from computers and capacitors to landing man on the moon and the supercomputers we use today. Understanding concepts about semiconductors such as the temperature-dependence of electron transmission Faraday discovered or electron transfer across junctions and how to facilitate them allow us to develop better devices whatever the end goal may be.

Semiconductors are unique based on their band gap and their atomic number. From these two basic characteristics are derived others such as mobility of charge carriers and p-type versus n-type for solar cells. Absorption coefficients will determine if the semiconductor is good for x-ray detection. Semiconductors can be used in electronics, transistors, and as radiation

detectors among many other uses. The best use for the material depends on the aforementioned properties. Semiconductors like cadmium telluride (CdTe) have shown to have useful applications as radiation detectors. Other factors such as cost and ability to grow high-quality uniform crystals in large quantities must also be considered for each application.

## 1.2 Solar Cells

Photovoltaics are a rising area of interest in research due to the concern of renewable energy sources. A photovoltaic cell uses sunlight to generate electricity. The efficiency of the cell depends on many factors with the infrared detector being the area with significant room for improvement. In the case of semiconductor-based solar cells for the absorption of light, possible materials for use are crystalline Si, amorphous Si, Se, Cu<sub>2</sub>S, Cu<sub>2</sub>O, InP, CdSe, Zn<sub>3</sub>P<sub>2</sub>, GaAs, Cu(In, Ga)Se<sub>2</sub>, and CdTe <sup>[1]</sup>. In order to have a useful material, the optical, chemical, and electronic properties must be taken into account. From the aforementioned list, the only possible semiconductors that may yield positive results based on past experiments are amorphous Si, CdTe, and Cu(In, Ga)Se<sub>2</sub> to replace the crystalline Si currently being used. This work focuses on cadmium telluride and its possibilities.

### 1.2.1 Anatomy of a solar cell

As depicted in Fig 1, a solar cell contains four major components: negative electrode, n-type semiconductor, p-type semiconductor, and a positive electrode. In practice, a solar cell will also contain a protective glass cover and an anti-reflective coating to increase efficiency. The n-type semiconductor contains a higher concentration of electrons; the p-type semiconductor contains a higher concentration of electron holes. The interface, called the np junction, allows

for a permanent electric field across the cell to be created. A semiconductor can be transformed into an n-type or a p-type material through doping. In order to form an n-type semiconductor, we must dope with a metal containing a higher number of valence electrons than the material. A p-type semiconductor will be doped with a metal with a lower number of valence electrons.

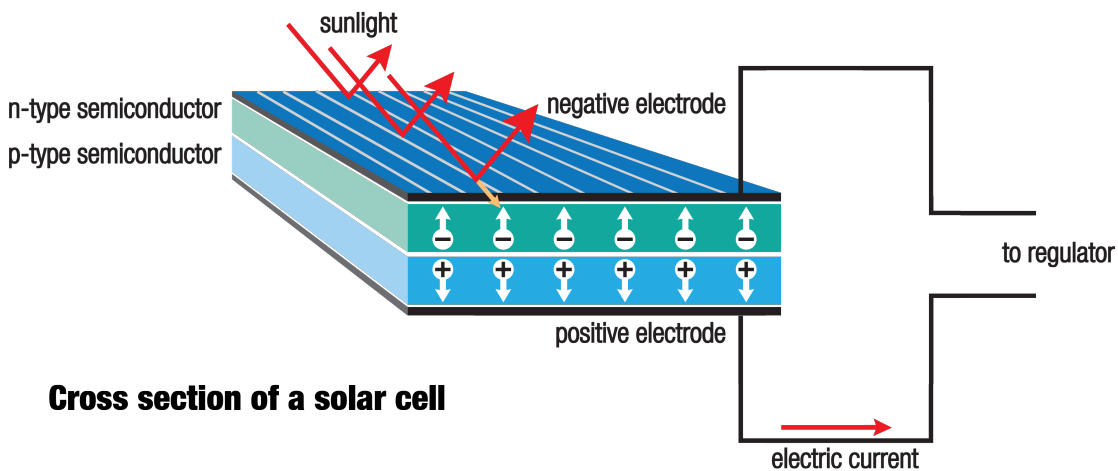


Figure 1-1: Cross section of a photovoltaic cell <sup>[1]</sup>

Commercially used solar cells use amorphous silicon doped with phosphorus for n-type and boron for p-type. Silicon contains four valence electrons and phosphorus contains five. The ‘extra’ electron will make for more electron-rich (phosphorus-doped) silicon. Boron has three valence electrons, one less than silicon, leaving a “hole.” These holes are positively charged due to the lack of the negative electron making the (boron-doped) silicon a p-type semiconductor. Because both are silicon, this qualifies a homojunction. A heterojunction is a junction in which the n-type semiconductor and the p-type semiconductor are different materials. An example of a heterojunction is CdS/CdTe.

When a photon is absorbed by the n-type semiconductor, an electron will absorb that energy and will be released into the p-type semiconductor via the photoelectric effect <sup>[2]</sup>. The n-

n-type semiconductor will now be positively charged and the p-type semiconductor will be negatively charged. These permanent charges create an electric field across the junction. As more electrons are knocked off of the n-type semiconductor, they will be guided to a wire forming a current via the electric field. In practice, multiple of these cells will be created to make a module and multiple modules will be connected to make an array, which are the commonly seen large panels <sup>[3]</sup>. The larger the array the greater current that can be produced.

As mentioned above, solar cells currently available use silicon as the semiconducting material. Since silicon is a material that has been widely researched, has a wide variety of application in electronics, and is low-cost, it was an obvious choice for use in photovoltaics. However, silicon has a low indirect energy band gap of 1.12 eV and therefore a low absorption coefficient of approximately  $10^4 \text{ cm}^{-1}$  <sup>[1]</sup>; these properties are not ideal for solar cells as they lead to low efficiencies. Other materials must be considered for solar cell improvement.

### 1.2.2 Cadmium telluride for future use in photovoltaics

A high absorption coefficient allows more photons to be available for conversion to electrical energy. The absorption coefficient is determined by the band gap of the material and whether it is a direct or an indirect gap. The simplified relationship between the absorption coefficient and the band gap of the material is as follows in Eq 1:

$$\alpha \approx \sqrt{h\nu - E_g}$$

where  $\alpha$  is the absorption coefficient and it is proportional to the square root of the difference between Planck's constant  $h$  times the light frequency  $\nu$  and the energy band gap  $E_g$ . It is easy to see from this relation that a small band gap will increase the absorption coefficient.

According to the research done by D. Bonnet and P. Meyers, the optimal band gap for a desirable absorption coefficient is of 1.5 eV <sup>[1]</sup>. Cadmium telluride is now the semiconductor of interest due to its direct band gap of 1.45 eV <sup>[1]</sup>. This band gap translates to an absorption coefficient greater than  $10^5 \text{ cm}^{-1}$  <sup>[1]</sup>. With this high of an absorption coefficient, the solar cell only needs microns of the material to absorb more than 90% of the available photons, which helps in reducing cost. According to the work done by P. Meyers, the most efficient CdTe cells came from high resistivity CdTe that were the best quality <sup>[4]</sup> to reduce dark current and device noise <sup>[5]</sup>.

Another aspect to consider when building a solar cell is stability. The sunlight that is absorbed by the semiconductor (cadmium telluride in this case) must be of lower energy than the energy required to break the chemical bonds of the material. The energy required to break the bonds in CdTe and CdS, used in conjunction with CdTe in solar cells, is greater than 5eV. The photons from sunlight carry energy lower than 5eV and are therefore unable to ionize the compound. This gives greater stability over time without concern over degradation <sup>[1]</sup>. When used in solar cell, cadmium telluride is typically doped to be a p-type and cadmium sulfide is doped to be an n-type.

### 1.3 Infrared detectors

The two types of infrared (IR) detectors are thermal detectors and photon detectors. Thermal detectors are the ones typically seen in infrared cameras and function by detecting a change in temperature of the material due to absorbed thermal radiation <sup>[6]</sup>. Semiconductor infrared detectors are photon detectors. A photon detector works by detecting a change in the electronic energy distribution due to the radiation absorbed interacting with the electrons in

lattice atoms, electrons in impurities, or free electrons <sup>[6]</sup>. The detector sends out a signal when an electronic energy distribution distortion is detected, which can then be recorded <sup>[6]</sup>. To quantize how well a photodetector works we use a factor called quantum efficiency. Quantum efficiency counts how many electron-hole pairs are generated for every incident photon of radiation <sup>[6]</sup>. The higher the quantum efficiency the better the photodetector.

A. Rogalski has determined the optimal conditions for an effective IR detector: the semiconductor should be lightly-doped semiconductor for IR absorption, electric contacts to the base of the detector should not contribute to the dark current of the device, and proper insulation must be present to prevent the generation of carriers <sup>[6]</sup>. Because IR detectors are commonly used in laboratories for systems with purpose of determining infrared absorption, for practicality IR detector size should be minimized and its durability maximized.

### 1.3.1 Cadmium telluride for use in infrared detectors

Cadmium telluride is a transparent material up to a thickness of 30 microns, is sturdier than silicon, and is already available commercially in large sizes making it an ideal substrate for epitaxial growth <sup>[7]</sup>. Unfortunately, pure cadmium telluride has proved to not be ideal for use in infrared devices. However, mercury doped cadmium telluride has been the subject of many projects due to some promising qualities as a consequence of its band structure and zinc-blende structure: the band gap can be tailored according to the thickness of it on the range of 1-30 microns, it has a large optical absorption coefficient giving it a high quantum efficiency, and it has a long carrier lifetime and operating temperature <sup>[8]</sup>. Mercury cadmium telluride (MCT) was first used in infrared technology in 1960 <sup>[6]</sup>. Recently, it has been investigated further

for the optimal Hg:Cd ratio of doping, which affects properties like bang gap, absorption coefficient, and quantum efficiency.

The band gap of the material determines the wavelength of light that will be absorbed. When light is absorbed, an electron will absorb that energy and will jump from the valence band to the conductive band as is characteristic of semiconductors. The size of the band gap in MCT can be changed by doping amount <sup>[8]</sup>. By selecting the size of the band gap, we are selecting the wavelength of the spectral region to suit our needs <sup>[7]</sup>. If the IR detector is used for IR absorption spectra, the detector can be made specific to select for the particular wavelength spectrum of interest.

As discussed in section 1.2.2, a high absorption coefficient of a material means that the material will absorb a larger fraction of available photons. The absorption coefficient can be calculated based on the band gap of the material. Depending on the size and doping amount, MCT has a direct band gap between zero and 1.5 eV. It has been determined that MCT has a large absorption coefficient and has a wide absorption band regardless of the polarization of light, a positive feature <sup>[6]</sup>. The quantum efficiency of a material is based on the absorption coefficient of the material. Rogalski has determined the quantum efficiency of MCT to be 70% without a reflective coating on the material and an impressive 90% with a reflective coating <sup>[6]</sup>. A higher quantum efficiency results in a more sensitive detector.

A common issue specific to photon detectors is reducing the temperature of the detector so as to reduce the background signal and receive a better true signal. On numerous occasions, the operating temperature of the semiconductor is well below room temperature increasing costs and complexity in the anatomy of the system. A common way to reduce the

temperature is through the use of liquid nitrogen at 77K, such as in the case of MCT. A proper operating temperature of the device leads to a high carrier lifetime. With a high carrier lifetime, there will be fewer electron-hole recombinations that don't belong to the photons being emitted by the object of interest, which gives an inaccurate signal.

### 1.3 Dosimetry

With the increasing widespread use of nuclear medicine, it is necessary to control the dose that is being delivered to the patient as well as the dose that the technician is being subjected to. The radiation that is the subject of concern is that from X-rays and gamma rays. It is well known that extensive exposure to ionizing radiation leads to the development of complications (i.e, cancer) years down the road. Nonionizing radiation is harmless and we can safely ignore it. Common imaging techniques such as computed tomography (CT), x-rays, and mammography use x-rays to form an image. Therapy techniques such as gamma-knife surgery for example and imaging techniques such as positron emission tomography (PET) involve gamma radiation. Radiation detectors serve the purpose of quantitatively monitoring exposure and dose delivered known as dosimetry.

#### 1.3.1 Basics of radiation detectors

There are three types of detectors: gas-filled detector, scintillator, and semiconductor detector <sup>[9]</sup>. A gas-filled detector is a device with two electrodes separated by a volume of gas; the *ionizing* radiation creates ions in the gas that are detected by the electrodes and expressed in the form of a current <sup>[9]</sup>. A scintillator works by producing ultraviolet or visible light as a result of interaction with ionizing radiation <sup>[9]</sup>. A semiconductor detector is a diode—an asymmetric



electrical device with a bias to pass current only when a certain voltage is surpassed and applied in one direction—with a small voltage applied in the direction “allowed” that will generate a momentary pulse of electrical pulse when electrons are excited in the material due to the radiation.

### 1.3.2 Properties needed for radiation detection

In order for us to develop an effective radiation detector, we must first understand the properties that are needed in the material. A radiation detector must be a semiconductor so that the photons that interact with it have energy comparable to the band gap and may be absorbed. The band gap of the material must be somewhat large to reduce thermally generated current that would otherwise lead to inaccurate readings. However, a small band gap results in a higher resolution due to low average ionization energy<sup>[10]</sup>. The ideal band gap for use in room temperature is between 1.35 and 2.55 eV<sup>[10]</sup>.

The energy carried by the photons that are absorbed by the material could result in Compton scattering. If the energy is not high enough for significant Compton scattering, the detector will work by the principles of photoelectric interactions. The latter is desirable for gamma-ray detection. A high atomic density ensures that photoelectric effect will dominate<sup>[10]</sup>. According to DS McGregor and H Hermon, the element in the semiconductor—most semiconductors for this purpose are comprised of two different elements—with a higher atomic density in the material will dominate, not the average of each of the atomic densities in the semiconductor<sup>[10]</sup>. This is a convenient property by which to preliminarily judge a semiconductor in comparison to others to determine if deeper exploration should be done.

A high quality material in large volumes that can be reproduced consistently is a concern for sustainability. A higher quality crystal will result in higher gamma-ray interaction efficiencies than its lower quality counterpart for obvious reasons. Because the detection of current is dependent on electron and hole mobility, the drift velocity will determine the extent to which the detector works. A long average free drift velocity is preferable for high resolution; a short average free drift velocity is convenient for quick measurements <sup>[10]</sup>. As already mentioned, these detectors are expected to be used in room-temperature environment, and so the operating temperature must be comparable to room temperature.

### 1.3.3 Cadmium telluride for radiation detectors

Research on cadmium telluride for its electrophysical properties has grown since the 1990s, but more recently it has been investigated for detection efficiency and dosimetry. In order for cadmium telluride to have possible applications as a radiation detector, it must have the appropriate density of electrically active dopants and imperfections <sup>[11]</sup>. Since the detector would be used in clinical settings, it is also necessary that it operate under room temperature conditions, which research seems to indicate that it does <sup>[12]</sup>. The high atomic number of tellurium ( $Z=52$ ) ensures that photoelectric effect will dominate over Compton scattering <sup>[10]</sup>.

The detectors investigated by AV Rybka *et al.* are p-type cadmium telluride crystals. A p-type crystal has a higher concentration of holes (positive) whereas an n-type semiconductor has a higher concentration of electrons (negative). The detectors must deal with gamma radiation with energies up to 3MeV, an energy range typical of nuclear waste <sup>[11]</sup>. For clinical purposes, the detector will have to measure both the current pulses per unit time—known as counting mode—and the average current over time—known as integration mode.

Metal-semiconductor-metal (MSM) detectors that used CdTe as the semiconductor have an overall resistance dependent on the bulk resistance of the semiconductor and the resistance of the metal contacts. The metal contacts on opposite sides are diodes, one forward-biased and the other reverse-biased. These detectors were subjected to both counting mode and integral mode to test their efficacy.

According to the research by AV Rybka *et al.* the use of the cadmium telluride detector as a solid-state ionization chamber has optimal working conditions in the bias voltage range between 20 and 80 V <sup>[11]</sup>. For a detector to be practical in count mode, it must have a linear relationship between count response and dose rate. This is a way of testing the sensitivity of the detector over a broad range of voltages. In preliminary tests, a radioactive isotope with known decay is used and the dose and response is plotted. It was found that CdTe had a strong linear dependence between dose rate and count rate <sup>[11]</sup>. This is, of course, a desirable trait for the accuracy of the dosimeter.

When in current mode, the dosimeter works by determining the formation and recombination rates of electrons and electron holes <sup>[11]</sup>. The current comes from the movement through the electric field created by the bias voltage applied to the detector. As tested by AV Rybka *et al.* in the voltage range of 80 to 150V, the current output had a linear relationship to the voltage signifying a consistency needed for practical applications <sup>[11]</sup>.

#### 1.4 Digital radiography

Radiography refers to the practice of producing an image from a three-dimensional object, in our case a patient, with the use of x-rays. The x-rays can be absorbed by the object or can be transmitted. The density and composition of each tissue (e.g, bone, muscle, fat) will

determine the interaction with the x-ray. The radiation that passes through the object is collected by a detector on the other side. Early radiography used screen film for the collection of those x-rays; this was used for most of the 20<sup>th</sup> century <sup>[9]</sup>. A downfall of screen-film radiography is the time that it takes to process the film as well as the quality of the image. To combat this, digital radiography has been developed.

In addition to being quicker, digital radiography has the advantages of having a reduced patient dose, better information archiving, elimination of processing cost, and lack of deterioration of the image over time <sup>[13]</sup>. A digital radiographer uses a radiation detector to collect the x-rays on the other side of the patient. It does so more quickly and efficiently than a screen film would. The radiation detected by the detector can then be converted to an image with the use of computer programs. Unlike a screen film, a digital radiograph does not develop a “shadow” through years of use, also an advantage to switching to digital.

#### 1.4.1 X-rays

Pulsed chest X-ray scans can be made with the use of a CdTe detector, which several labs are already testing. One research lab used the detector in counting mode (as explained in section 1.3.3) for a dual-energy X-ray multi-detector scanning system <sup>[14]</sup>. The result was an average energy resolution of 5.1% keV for 60 keV rays with the counting varying by 11% <sup>[14]</sup>.

#### 1.4.2 Computed Tomography

An increasingly common imaging technique called computed tomography, known as CT, uses x-rays to form an image and reconstruct a three-dimensional representation of the body for various diagnostic purposes. CT images are also fused with positron emission tomography

(PET) images to have better anatomy in the combined image in comparison to the PET image alone. Cadmium telluride detectors and zinc-doped cadmium telluride detectors have been investigated since the early 1990s<sup>[13]</sup> but there are limitations to long-term use that need to be further investigated.

### 1.5 Cardiac function monitoring

A nuclear stethoscope uses a gamma camera and a radioactive substance in the body to form images of certain organs. It is most commonly used for ventriculography (the imaging of the left or right ventricle of the heart) and myocardium (the muscle in the heart) defect monitoring although it can also be used for imaging of the breast or brain among others. A contrast is injected into the patient that “marks” red blood cells; the gamma camera then detects the gamma rays emitted by the radioactive contrast and forms an image from said gamma rays. The device needs to be light, portable, and small for its use to be convenient. This is a painless, non-invasive procedure, which is preferable to invasive procedures due to time and safety concerns.

#### 1.5.1 Current gamma cameras

Current systems have gamma cameras that use sodium iodide (NaI) as the detector and thallium as the contrast. The biggest improvements to be made are to the poor resolution and rather large size<sup>[15]</sup>. The head of the camera has dimensions of 40x50x0.9 cm<sup>3</sup><sup>[15]</sup>, which is understandably cumbersome to use. A smaller camera allows closer proximity to the organ of interest thereby increasing the quality of the image. A better detector would increase the

resolution while simultaneously reducing the dose delivered to the patient, both of which are always improvements looking to be made.

#### 1.5.2 Cadmium telluride for use in gamma cameras

Among other semiconductors, cadmium telluride is a good choice to replace sodium iodide because of the relatively small crystal size needed <sup>[15]</sup>. Aside from these physical attributes, cadmium telluride provides good energy resolution with excellent spatial and contrast resolution <sup>[15]</sup>. The first prototype of its kind was created by the Nuclear Medicine Department of the State Cardiology Hospital of Balatonfüred in Hungary <sup>[16]</sup>. However, they ran into multiple issues: the gamma camera was sensitive to the positioning on the chest wall to thoracic motion and the background radiation from other blood paths <sup>[16]</sup>.

For use with cadmium telluride detectors the contrast is best replaced with technetium-99m. This radioisotope works in the same way as the thallium: it marks red blood cells so that the radiation follows the blood pathways. These new CdTe detectors are 2mm thick (compared to 9mm with NaI), have a 70% counting efficiency with <sup>99m</sup>Tc gamma emission energy of 140 keV, and exhibits no polarization effects at 30V bias voltage <sup>[16]</sup>. As mentioned before, photons with the ability to induce Compton scattering are problematic for the contrast to noise ratio of the image. Unlike sodium iodide, cadmium telluride detectors are effective in the scatter rejection of these photons <sup>[15]</sup> to deliver a higher-quality image.

#### 1.6 Concluding remarks

A significant limitation to the use of cadmium telluride for any of the above purposes is the difficulty of growing high-quality material in large volumes. A common tactic to resolve this

is to dope the material with other elements to increase the large-scale quality. For cadmium telluride, common dopants are mercury, zinc, and chlorine. Mercury-doped cadmium telluride is commonly used in infrared detectors and solar cells. Zinc-doped cadmium telluride is commonly researched alongside cadmium telluride for use in gamma- and X-ray detectors<sup>[11, 13, 14]</sup>. Chlorine-doped cadmium telluride has applications in nuclear detection<sup>[17]</sup>. Doped materials can also act as a buffer layer between the substrate—silicon for this work—and the material being grown—cadmium telluride—to reduce lattice mismatch. Reducing the lattice parameter mismatch relieves the material grown from stress while mostly retaining its properties. As discussed in previous sections, doping allows for different behaviors of the material such as electron-rich versus hole-rich and adjustable band gap. Adjusting dopants gives more control to achieve the desired results.

The CdTe grown for this project is to be used as infrared detectors and in solar cells. In the future, we hope to advance to doping of the material for more practical behavior for the purpose.

### 1.7 Limitations of widespread use of cadmium telluride

Although advancements have been made in science for the use of CdTe in photovoltaic modules and such, we must still take into account the practicality aspect of using CdTe for more than just in the lab. We have already made advancements in the size of crystals grown and in efficiencies of the solar cells. However, we have to take into account the environmental and health impact of using such elements, the cost of the materials, and what to do with the material after it has fulfilled its purpose.

### 1.7.1 Cadmium toxicity

Heavy metals, such as cadmium, have been known to have adverse health effects on the human body. Observed effects include damage to the central nervous, cardiac, and gastrointestinal systems; harm to the liver, kidneys, lungs, endocrine glands, and bones; and even increased risk of some forms of cancer<sup>[18]</sup>. Heavy metals can make their way into the body through ingestion, absorption, injection, and inhalation. In the production of CdTe solar cells, there is concern for environmental release of cadmium through accident or fire and worker exposure to cadmium through working conditions<sup>[1]</sup>. Fortunately workers have experienced no unusual uptake of cadmium due to factory conditions<sup>[1]</sup>. Fire of a solar panel leads to no release of cadmium because the glass melts before CdTe decomposes and the liquid glass serves to shield CdTe panel from fire<sup>[1]</sup>. Since cadmium never makes it to the environment, discussing environmental impact is unnecessary.

### 1.7.2 Limited supply of tellurium

Although tellurium is an abundant nonmetal in the universe, it is a limited resource on Earth. As of 2010, generating one gigawatt of power from a CdTe solar cell requires 91,000 kilograms of tellurium for a cost of about \$20 million<sup>[19]</sup>. As tellurium is used for PV, the market price will increase due to simple supply and demand leading to an increase in the overall price of the cell. Currently, Te is currently obtained as a byproduct of the refining of copper from the earth's crust<sup>[19]</sup>. Mines in China, Mexico, and Sweden have shown to have a rich tellurium concentration along with bismuth, which is a possible source for obtaining Te<sup>[19]</sup>. We are on our way to remedy the Te supply issue by making thinner, more efficient cells.



### 1.7.3 Recycling of solar cells

Fortunately, the aforementioned issues can be partially offset by the recycling of CdTe, specifically the photovoltaic modules. It is possible to extract and separate Cd and Te from each other, which can then be reused. There are four ways currently being investigated for dealing with CdTe module waste: leaching with  $\text{LiCl}_3/\text{HCl}$  solution, oxygen-pressure leaching using  $\text{H}_2\text{SO}_4$ , leaching with  $\text{HNO}_3$ , and leaching with  $\text{H}_2\text{SO}_4/\text{H}_2\text{O}_2$  solution <sup>[20]</sup>. Each of these methods leaches one of the elements from the compound and the other is recovered using electrolysis, electrowinning, or ion-exchange methods. Leaching methods can also be used to recover the glass cover from the cell.

## Chapter 2: Methodology

### 2.1 Introduction to Spectroscopic Techniques

Spectroscopy is a commonly used technique for analyzing substances using electromagnetic radiation (i.e, light). When light interacts with a substance, the following mechanisms occur: transmission, absorption, or reflection. The interaction is determined by the energy of the photons, types of functional groups present, bond strength, bond length and angles, concentration, morphology, chemical composition among other characteristics on the atomic scale. When a substance is irradiated, the photons will interact with the substance in a particular and specific fashion according to the aforementioned properties. Similar to a fingerprint, interactions are unique and will give data that is used for quantitative and qualitative purposes. It is necessary to understand that each technique will provide limitations on the output of data and it is therefore beneficial to use more than one technique for a complete characterization of a substance.

By the nature of the structure and chemical composition of substances, some characteristics will only be evident by the transmission and absorption of electromagnetic radiation in the form of light while others will only be evident by the scattering (reflection) of light. Fourier Transform Infrared (FTIR) and Confocal Raman (Raman) spectroscopies complement each other well for a complete picture in that the former uses transmission and absorption of light and the latter uses scattering of light for their respective spectra. The current work is mainly concentrated on Raman and FTIR techniques. Other microscopic techniques include Scanning Electron Microscopy (SEM), Transmission Electron Microscopy

TEM, and Scanning Tunneling Microscope (STM), all of which provide their own advantages and disadvantages.

## 2.2 Raman Spectroscopy

Raman spectroscopy was developed based on the discoveries made by Dr. Sir Chandrasekhara Venkata Raman on the scattering of light, who received a Noble Prize for Physics in 1930<sup>[21]</sup>. The light scattering can be due to either elastic collisions or inelastic collisions, the latter being of interest for spectroscopic purposes<sup>[22]</sup>. Because light can be interpreted in its classical representation of a wave and in its quantum interpretation of a particle, both approaches can be used for explanation of how Raman spectroscopy works.

During an inelastic collision, kinetic energy is not conserved. The change in kinetic energy, whether it is up or down—called Raman scattering—is unique to a material and can therefore be used for characterization. The interaction of light with the material is due to vibrations, rotations, and low-frequency transitions in molecules<sup>[23]</sup> and is what results in the change of energy measured. If the scatter does not result in a change of kinetic energy, an elastic collision called Rayleigh scattering is occurring<sup>[24]</sup>. These elastic collisions provide no information because there was no excitation of the molecule. The use of this spectroscopic technique relies on the existing literature of photon interactions with materials. The established values of energy absorption and transfer allows us to do the characterization of materials.

### 2.2.1 Classical Wave Representation of Raman Scattering

In the classical representation the oscillating electric field component of light will interact with the electron cloud of the molecule resulting in polarization of the molecule. The

polarization of a molecule is the induced dipole moment that occurs when there is an unequal distribution of positives and negative in the molecule. The dipole moment is mathematically described by Eq. 2:

$$\vec{p} = \vec{\alpha}(Q) \cdot \vec{E}$$

$$p = \alpha(Q)E_0 \cos(\omega_L t)$$

where  $\vec{p}$  is the resulting dipole moment,  $\vec{\alpha}$  is the polarizability,  $\vec{E}$  is the electric field with maximum amplitude  $E_0$ , and  $\omega_L$  is the angular frequency of the incident light<sup>[25]</sup>.

In Eq 2 above, the polarizability,  $\vec{\alpha}(Q)$ , is represented by a tensor that is dependent on the vibrational coordinate  $Q$ , which is an indicator of the deformation of the electron cloud in the presence of an external electric field. This vibrational coordinate is dependent on other factors as well depicted by Eq 3:

$$Q = Q_0 \cos(\omega_M t)$$

where  $Q$  is the vibrational coordinate with maximum  $Q_0$  and dependent on the molecular vibrational angular frequency  $\omega_M$ <sup>[25]</sup>. We can see from Eqs 2 and 3 that a change in polarizability results in a change in amplitude at certain frequencies of the induced dipole moment and the combination of these aforementioned changes results in Raman scattering. Eq 4 shows a Taylor expansion of the polarizability:

$$\alpha = \alpha_0 + \left[ \frac{\partial \alpha}{\partial Q} \right] Q + \dots$$

and substituted into Eq 2 to give Eqs 5a and 5b

$$p = \alpha_0 E_0 \cos(\omega_L t) + \left[ \frac{\partial \alpha}{\partial Q} \right] Q E_0 \cos(\omega_M t) \cos(\omega_L t)$$

$$p = \alpha_0 E_0 \cos(\omega_L t) + \left[ \frac{\partial \alpha}{\partial Q} \right] Q E_0 \cos[(\omega_M - \omega_L)t] + \left[ \frac{\partial \alpha}{\partial Q} \right] Q E_0 \cos[(\omega_M + \omega_L)t]$$

We can analyze this equation term by term as each conveys different interactions. The first term expresses an elastic Rayleigh collision in which no change in frequency occurs. The difference in the argument of the cosine in the second term expresses a decrease in frequency of the light, which indicates inelastic Stokes scattering<sup>[26]</sup>. During Stokes scattering, the light emitted carries less energy than the light that was absorbed. The last term denotes an increase in frequency of light, which occurs much less frequently, to indicate inelastic antiStokes scattering<sup>[26]</sup>. AntiStokes scattering occurs when the light emitted is at a higher energy due to absorption of energy from the material. These changes in frequency are important because they are indicative of an interaction with the molecule. As previously stated, Raman spectra is concerned with the inelastic scattering of light and therefore we are only concerned with the latter two terms.

### 2.2.2 Quantum Particle Representation of Raman Scattering

For the quantum representation, we are dealing with a light particle called a photon that itself carries energy. Just like in the classical interpretation, we have an inelastic collision that results in a change in energy. Fig 2-1 is a schematic representation of the incident and scattered photons during measurement.

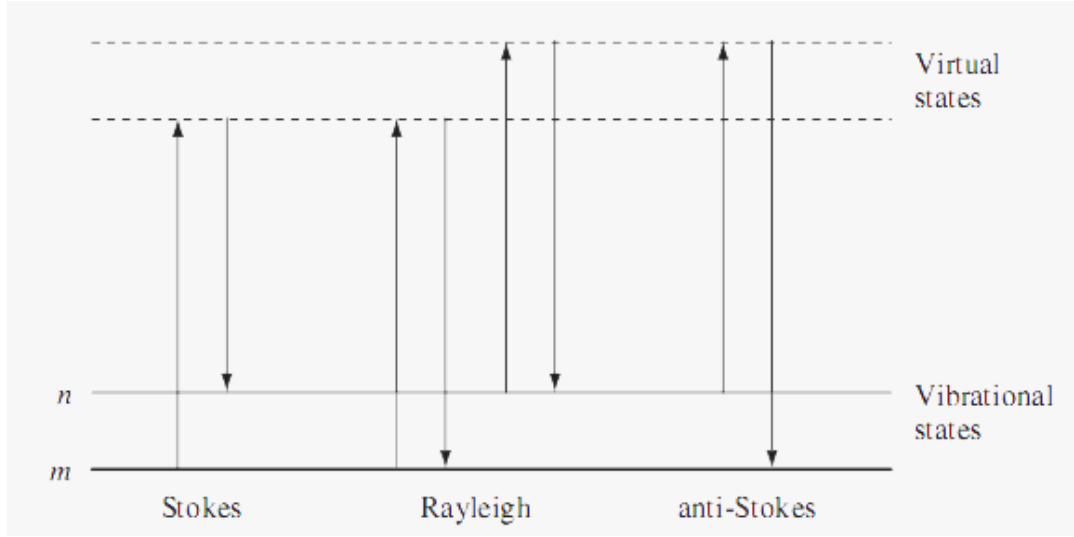


Figure 2-1: Rayleigh, Stokes, and antiStokes scatters according to energy transfers.<sup>[27]</sup>

As mentioned before, we are interested only in the inelastic collisions, which are Stokes and antiStokes. During Stokes scattering, some of the energy of the photon is transferred to the substance, and the inverse occurs in antiStokes scattering. Typically, the material will be in its ground state meaning that it has no energy to give to the photon. Consequently, antiStokes scattering is rare to observe. As a result, Stokes scattering is what we become concerned with for Raman although we will discuss the physics of antiStokes scattering as well.

Through these energies, we deduce what we call Raman shift as represented by Eq 6:

$$\frac{\Delta\omega}{2\pi c} = \left( \frac{1}{\lambda_L} - \frac{1}{\lambda_S} \right)$$

where  $\Delta\omega$  is the Raman shift,  $c$  is the speed of light in vacuum,  $\lambda_L$  is the excitation wavelength, and  $\lambda_S$  is the scattered wavelength<sup>[25]</sup>.

During Stokes scattering, a photon with frequency  $\omega_L$  strikes the material and transfers part of its energy scattering with frequency  $\omega_L - \omega_M$ <sup>[26]</sup>. The transfer of energy causes the atoms in the molecule to vibrate. During antiStokes scattering, a photon strikes the surface of the

material with frequency  $\omega_L$  and absorbs energy from the material scattering with frequency  $\omega_L + \omega_M$ <sup>[26]</sup>. This absorption of energy indicates that the material was not previously in its ground state.

Since in Raman, 999,999 photons for every 1,000,000 will undergo Rayleigh scattering and only 1 of 1,000,000 will undergo inelastic scattering. The Raman signal is usually weak. Thus, to distinguish it from the very strong Rayleigh scattering signal performant systems are needed. To increase the quality of the Raman spectrum we can either use a high-resolution filter for better detection of the 0.001% of the photons we are interested in or we can reduce the number of Rayleigh scattered photons through notch filters, tunable filters, laser stop apertures, and double and triple spectroscopic systems giving us an increase in the ratio of inelastically scattered photons to total scattered photons yielding a better image.

### 2.2.3 Experimental Set Up

The measurements in the current work were performed using an alpha 300 WITec confocal Raman system. The 532 nm excitation of an Nd:YAG laser was employed. Pictured below is the system as set up in the Optical Spectroscopy and Microscopy Laboratory where data was collected.

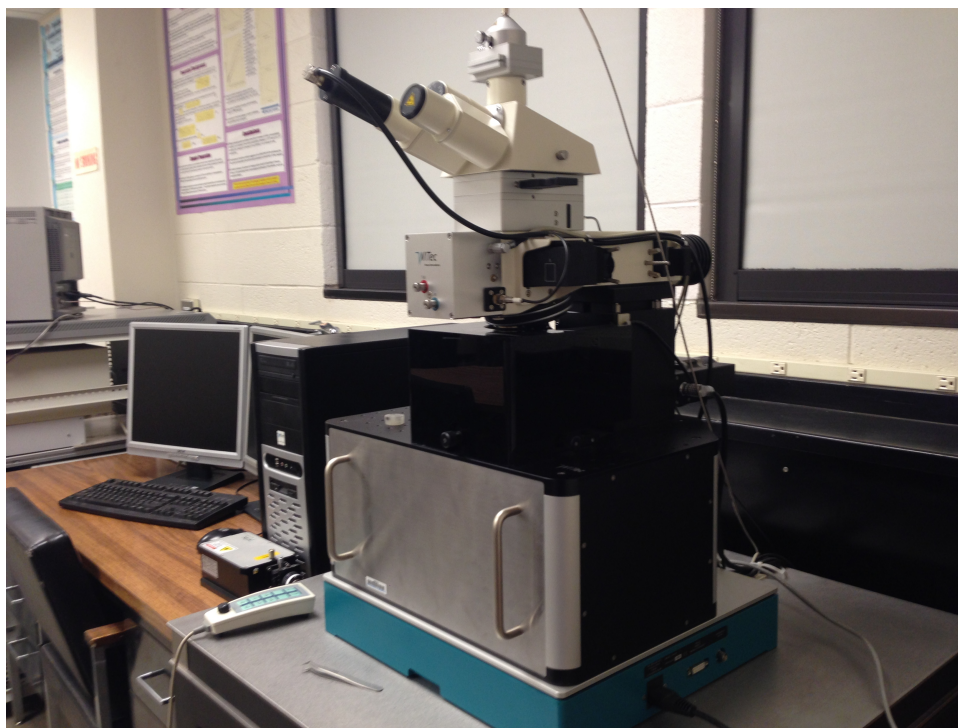


*Figure 2-2: Confocal Raman Spectroscopy and Microscope by WiTec*

### 2.3 Fourier Transform Infrared Spectroscopy

Fourier transform infrared spectroscopy (FTIR) uses infrared radiation, a Michelson interferometer, and Fourier transform to create a spectrum that can be analyzed to determine functional groups present, chemical compounds, and molecular structure of organic and inorganic materials. Each group of interest will have a specific line of absorption (wavenumber) at a specific location. Therefore, we can use the spectrum for specific characterization of a material. The first FTIR system was used by Perkin-Elmer in 1957 with a sodium chloride crystal as a beam splitter<sup>[28]</sup>. Crystals later used include potassium bromide and cesium iodide. As improvements have been made we have furthered our understanding of infrared systems. Optimization of collected data through a wide range of infrared detectors and beam splitter have been accomplished.



### 2.3.1 The Michelson Interferometer and Interpretation of Data

As the name suggests, FTIR spectroscopy uses an infrared source as electromagnetic radiation. The Michelson interferometer was developed by Albert Abraham Michelson in 1887<sup>[29]</sup>, who also made several other developments for optics. The Michelson Interferometer uses a beam splitter (a crystal) to split the beam into two beams that will recombine. The constructive and destructive interferences are the key to the Michelson Interferometer. Fig 2-3 is a schematic representation of the Michelson Interferometer.

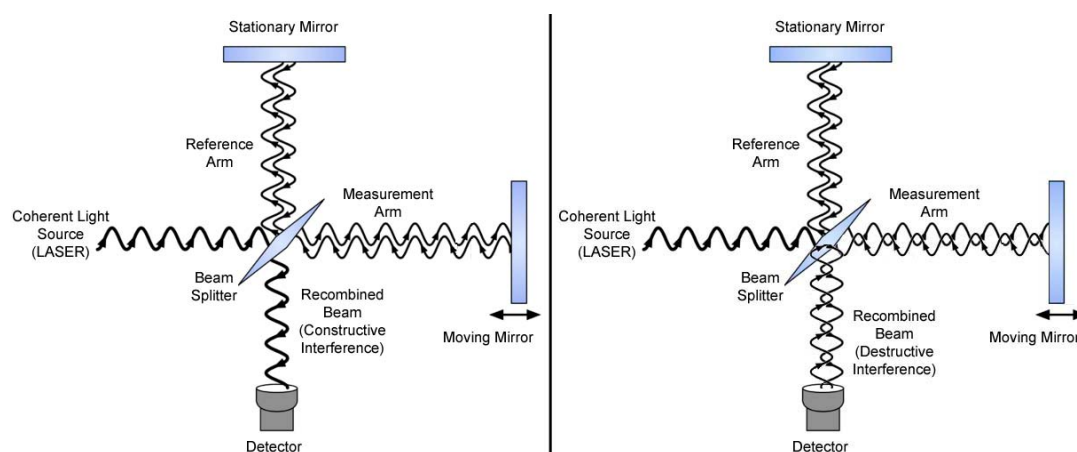


Figure 2-3: Schematic representation of Michelson Interferometer<sup>[30]</sup>

The path begins at the “Source” where a laser is emitted. When it reaches the beam splitter, the laser beam will split so that half of the photon beam changes trajectory towards the movable mirror traveling a distance  $L + \delta x$  and the rest continue towards the fixed mirror traveling a distance  $L$ . When each of these beams hits the respective mirror, they will reflect, being on their way back to the beam splitter once again. The beam that reflected off of the movable mirror will travel a distance  $L + \delta x$  in its return path, while the beam reflected from the fixed mirror will travel a distance  $L$ . When the two beams hit the beam splitter, they will recombine into a single beam.

When two waves come together in such a manner, they will have constructive interference, destructive interference, or somewhere in between. For the FTIR, only constructive interference is of use. The optical path difference—that is the difference between  $2L$  and  $2(L+\delta x)$ —and the wavelength  $\lambda$  of the laser will determine whether the waves will have constructive or destructive interference according to the following relationships:

$$2\delta x = n\lambda \quad n = 1, 2, 3, \dots$$

$$2\delta x = 0.5m\lambda \quad m = 1, 3, 5, \dots$$

By simple inspection, we can see that the first equation describes constructive interference and the second describes destructive interference. During constructive interference, we would see a bright spot on a screen; during destructive interference we would see a dark spot on the screen. Maximum intensity happens during constructive interference in which there is no path difference aptly named Zero Path Difference (ZPD) where  $\delta x$  (the path difference) is equal to zero.

When the Michelson Interferometer is put into use for FTIR, the material is placed immediately before the detector. For more accurate measurements, a “background” is run. The background serves as a reference for the rest of the measurements; we will refer to the intensity as  $I_0$ . The measurements done with the sample in place following the background will use this  $I_0$  to determine the intensity of the light that is absorbed and the intensity of the light that is transmitted—denoted by  $I_T$ —as depicted in Fig 2-4. A small portion of photons are reflected and are negligible for our purposes.



Figure 2-4: Incident, reflected, and transmitted light interactions with a sample<sup>[25]</sup>

The relationship between the incident light  $I_0$  and the transmitted light  $I_T$  is known as Bouguer-Lambert-Beer law<sup>[31]</sup> given by Eq 7:

$$I_T = I_0 e^{-\alpha d}$$

where  $\alpha$  is the linear absorption coefficient of the material at a specific wavenumber and  $d$  is the thickness of the sample. The transmitted photons will reach the detector and be used for the interferogram. The interferogram is the plot of detector response (i.e. photons counted) as a function of optical path difference. The interferogram uses Fourier Transform to interpret the data to produce sensible results.

Although the detector is using the transmitted photons for the interferogram, the absorbed photons are the photons of interest seeing as how they are the ones that are interacting with the substance. The absorption of photons will appear as a peak in the interferogram. When the material absorbs a photon, it is being excited from energy state  $E_0$  to energy state  $E_1$ . The energy absorption is related to the wavelength of the photon by Eq. 8:

$$E_1 - E_0 = hc/\lambda$$

Where  $h$  is Planck's constant of  $6.626 \times 10^{-34}$  J·s,  $c$  is the speed of light in vacuum of  $3.00 \times 10^8$  m/s, and  $\lambda$  is the wavelength of light in meters.

The energy absorbed is generally between one and ten kilojoules per mole. This energy band corresponds to the spectrum of  $13,000$  to  $10 \text{ cm}^{-1}$  wavenumbers. The ideal range of the electromagnetic spectrum for this kind of measurements is therefore the infrared spectrum.

Within the infrared spectrum exist near infrared (NIR) in 12500 to 4000  $\text{cm}^{-1}$ , mid infrared (MIR) in 4000 to 400  $\text{cm}^{-1}$ , and far infrared (FIR) in 400 to 5  $\text{cm}^{-1}$ . Each one of these bands of frequencies carries different energies, but they will overlap in transitions. Although we make measurements using only one (NIR, MIR, or FIR) at a time, it is useful to repeat measurements in a different band of IR to get a more complete picture.

### 2.3.2 Experimental Set up

The system used for this work is a vacuum based Bruker IFS 66v. Figs 2-5 and 2-6 below depict the inner set up of the system as provided by Bruker and the view from outside. The main components of the system are the interferometer, collimator, fixed mirror, moving mirror, beam splitter, broad lamp source for alignment and laser for measurements.

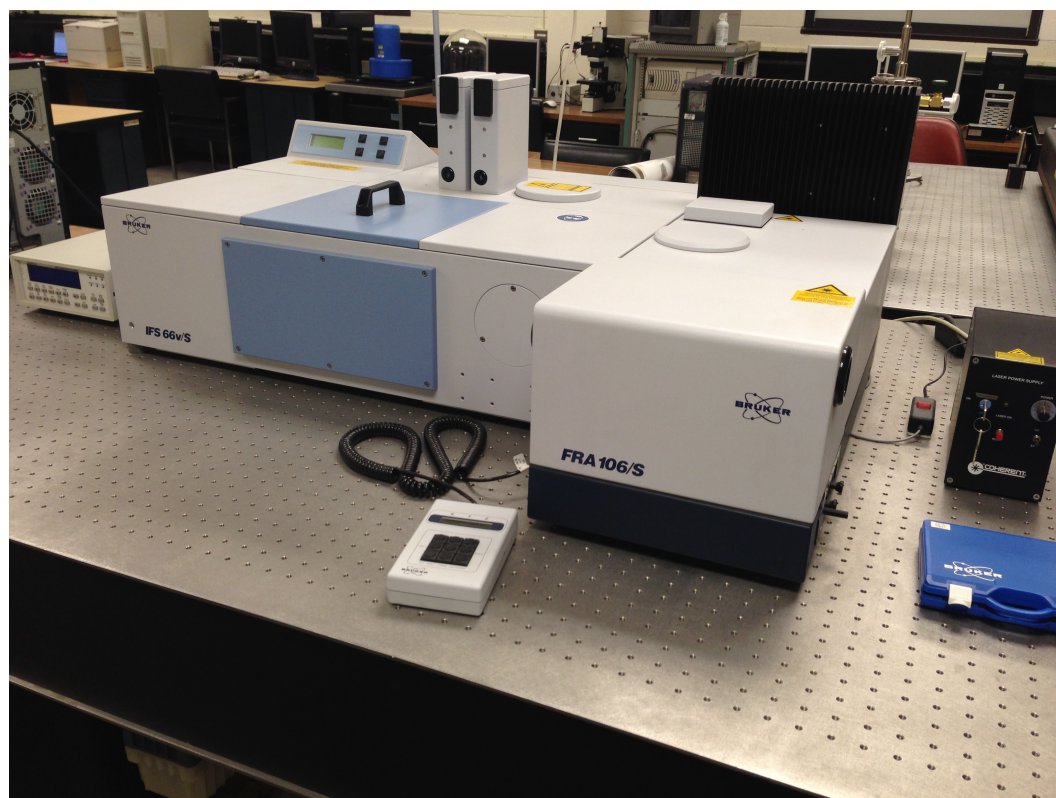


*Figure 2-5: Fourier Transform Infrared Spectroscopy by Bruker*

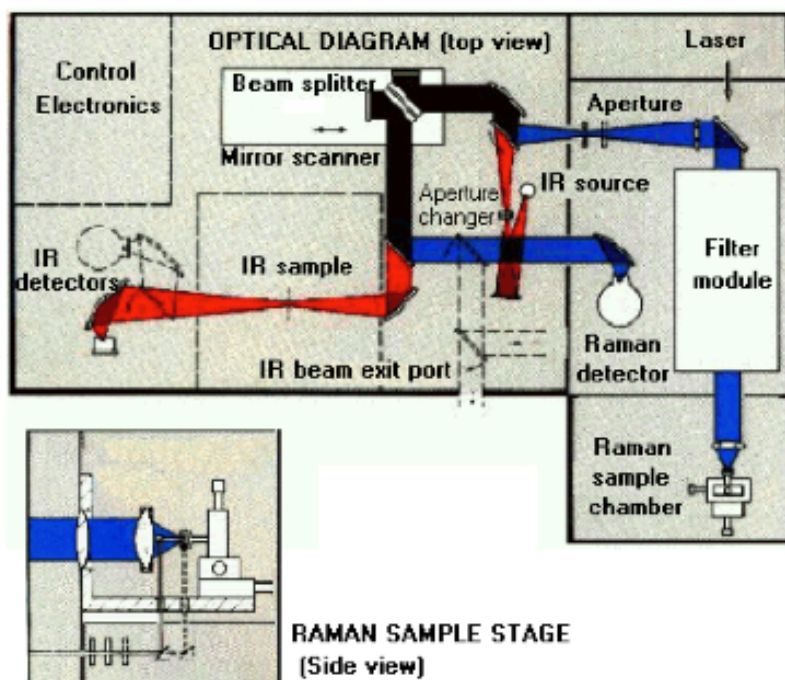


Figure 2-6: Bruker FTIR optical path

As seen in Fig 2-6, the main components and their purposes are as follows:

- Source: black body source emits infrared radiation that passes through an aperture to control exposure to the sample
- Interferometer: based on the Michelson Interferometer to provide path of radiation
- Sample: in the sample chamber at a fixed position
- Detector: most commonly a semiconductor for the recording of photons to the transformed into interferogram
- Computer: compiles, records, and interprets data to output interferogram

FTIR is based on the principle that there exist specific shapes and wavenumbers of absorption for functional groups, bonds, and so on as previously mentioned. For this reason, the success of FTIR relies of previously acquired data. Practically speaking, the interferogram

given by the computer must be compared to existing data to assert that what we are seeking is present; it would be impossible to do so without the existing literature.

For the work present, we have used a Globar lamp, which is a silicon carbide rod that operated in a range of 20 to 10,000  $\text{cm}^{-1}$ . The beam splitter used was a Ge-coated mylar beam splitter whose optimal range is 20 to 700  $\text{cm}^{-1}$ . The detector we have used is a deuterated, L-alanine doped triglycine sulfate (DLaTGS) that operates at room temperature with a range of 10 to 700  $\text{cm}^{-1}$ .

## 2.4 Comparison of Raman and FTIR

As previously mentioned, FTIR and Raman are rarely individually used as the sole method for characterization. FTIR and Raman use different principles: FTIR uses absorption to compile data whereas Raman uses scattering, a form of reflection. Not all molecules will react to one, the other, or both and it is therefore necessary to use both methods. For instance, a symmetric, diatomic molecule will not exhibit changes in its dipole moment, which is a necessity for infrared absorption spectra and therefore we would expect an indistinct infrared spectrum. However the molecule will exhibit a change in polarizability due to the interaction of the electrons with the nucleus from the stretching and contracting of the bonds. Because there is a change in polarizability, we will be able to produce a Raman spectrum.

If we were to characterize a highly symmetric polyatomic molecule, such as a cycloalkane, we would use FTIR because it has an active IR band but an inactive Raman band. A molecule containing carbonyls or nitriles can be characterized using FTIR, whereas we would need Raman for aromatic rings and carbon-carbon pi bonds. However, molecules with little symmetry will exhibit behavior that can be detected by both Raman and IR. In general, we can

use FTIR for asymmetric molecules that will express changes in dipole moment and Raman for symmetric molecule that will experience a change in polarizability.

Different parts of the electromagnetic spectrum will interact with samples differently due to different energies. The band of wave numbers including visible light and ultraviolet light will result in fluorescence and photoluminescence. Because FTIR uses infrared light exclusively, these are not an issue for this kind of spectroscopy. However, because Raman uses near IR, the possibility of fluorescence and photoluminescence increases. To reduce the likelihood of this happening, Raman uses NIR laser diodes to avoid it giving us a higher quality picture.

Although this work is not directly affected by it, water used as a solvent for samples will affect the FTIR spectrum. Water is a strong mid IR absorber but it is a weak Raman scatter therefore Raman is a better choice for aqueous solutions and biological systems.

In summary, the advantages to FTIR are:

- High quality of data for a full energy range
- No interference due to fluorescence
- Quick output of data

The advantages to Raman are:

- Provides mapping that FTIR does not
- Can be used with aqueous and biological compounds
- Provides information on stress and strain of the sample

## 2.5 Sample Preparation

The samples were grown in Dr. Stella Quinones's laboratory at the University of Texas at El Paso by graduate student Aryzbe Diaz. Si(111) and Si(211) substrates 1 cm x 1 cm were

patterned using the photolithography technique, resulting in a pattern transfer with photoresist islands 2  $\mu\text{m}$  in diameter with a 2  $\mu\text{m}$  pitch. Si pillars were created by dry etching the patterned surface using an Oxford Plasma etcher. Sulfur hexafluoride ( $\text{SF}_6$ ) gas was used to achieve isotropic etch of the Si surface. Si pillars of 2  $\mu\text{m}$  diameter were etched into the Si surface and further reduced to range of 1  $\mu\text{m}$  – 500 nm. The patterned substrates were cleaned prior to CdTe deposition by immersion in a piranha solution  $\text{H}_2\text{SO}_4\text{:H}_2\text{O}_2$  with a ratio of 5:1 for 10 min at 130°C, followed by immersion in a buffer oxide etch BOE solution for 10 s to remove the native oxide. Selective CdTe growth was performed using a conventional CSS reactor. Helium (He) was used as a carrier gas in the CSS vacuum chamber. A single crystal CdTe source containing twins was annealed for 30 min. at 600°C prior to each deposition to remove the thin oxide layer in order to produce repeatable growth rates for each set of experiments. Several sets of experiments were performed by varying the source temperature, substrate temperature, and system pressure to observe the effect of these parameters on the quality growth. The following table includes the set of experiments performed for the CdTe/Si(111) and CdTe/Si(211) films.

*Table 2-1: Growth parameters*

<b>Si(111) and Si(211) Samples</b>						
<b>Sample</b>	<b>Pattern Size</b>	<b>T<sub>sub</sub> (°C)</b>	<b>T<sub>sou</sub> (°C)</b>	<b>Pressure (Torr)</b>	<b>Dep. Time</b>	<b>Uniformity (Poor, Fair, Good)</b>
S111-2	1 $\mu\text{m}$	450	550	5	15 min.	Fair
S111-10	1 $\mu\text{m}$	450	550	2	5 min.	Fair
S111-12	1 $\mu\text{m}$	450	550	1	5 min.	Fair
S111-14	1 $\mu\text{m}$	450	550	0.5	5 min.	Good
S111-16	1 $\mu\text{m}$	450	550	0.25	5 min.	Good
S111-18	1 $\mu\text{m}$	450	550	1	5 min.	Poor



S111-23	1 $\mu\text{m}$	450	550	0.5	5 min.	Good
S111-25	1 $\mu\text{m}$	450	550	0.25	5 min.	Good
S111-1	500 nm	450	550	5	5 min.	Fair
S111-19	500 nm	450	550	2	5 min.	Fair
S111-17.1	500 nm	450	550	1	5 min.	Poor
S111-17.2	500 nm	450	550	0.5	5 min.	Good
S111-19	500 nm	450	550	0.25	5 min.	Good
S211-1	1 $\mu\text{m}$	450	550	0.5	5 min.	Good
S211-2	1 $\mu\text{m}$	450	540	0.5	5 min.	Fair
S211-3	1 $\mu\text{m}$	450	550	0.5	5 min.	Good
S211-5	1 $\mu\text{m}$	450	550	0.5	5 min.	Good
S211-8	1 $\mu\text{m}$	450	560	0.5	5 min.	Good

## Chapter 3: Results and discussion

### 3.1 Introduction to characterization of cadmium telluride

Because this work is based on classification by Raman spectroscopy and Fourier transform infrared spectroscopy (FTIR), this literature review focuses on those two. Scanning electron microscopy was used for imaging purposes and will therefore be briefly commented on. As a brief introduction, Raman spectroscopy is based on the scattering of light and FTIR is based on the absorption and transmission of light. A more thorough explanation is provided in chapter two.

The size, crystallinity, and indirectly the stoichiometry of a substance is determined by comparing the phonon modes in the samples grown to the phonon modes in the corresponding bulk material. A phonon is the quantum mechanical description of the vibrations of atoms within a material. Depending on the type of vibration, the phonons will be described as transverse acoustical (TA) mode, longitudinal acoustical (LA) mode, transverse optical (TO) mode, or longitudinal optical (LO) mode. Although not present in the bulk, surface (SO) phonons may also be observed in small crystals. Further discussion on SO phonons will come with the results. The known phonon modes exhibited by CdTe are shown in the table below as reported by EJ Danielewicz and PD Coleman <sup>[32]</sup>. We must also note that detecting multiples of the phonons, e.g, 2LO, TO+LO can occur. In such a case, the doublet of phonons is observed at the sum of their individual frequencies.

*Table 3-1: Frequency values exhibited by phonons in cadmium telluride*

Phononic Mode	LO	TO	LA	TA
Frequency ( $\text{cm}^{-1}$ )	148	139	97	35

### 3.2 SEM and Raman analysis of sample grown on Si(111)

Figs 3-1 and 3-2 respectively show an SEM and confocal Raman images of the sample containing CdTe grown on Si(111). These images show uniform growth of crystals between 2.3 and 4.8  $\mu\text{m}$  with clear grain boundaries. Because of the intended use, the smooth, flat surfaces within the crystals as seen in the SEM image demonstrate high quality of the crystals. We can also see that all silicon pillars in this section yielded growth of a crystal.

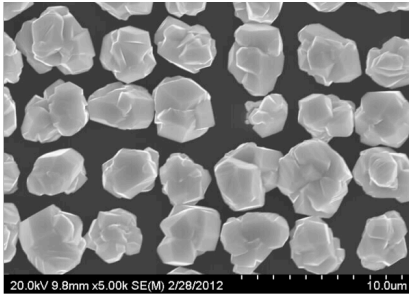


*Figure 3-1: SEM image of sample CdTe grown on Si(111) <sup>[40]</sup>*

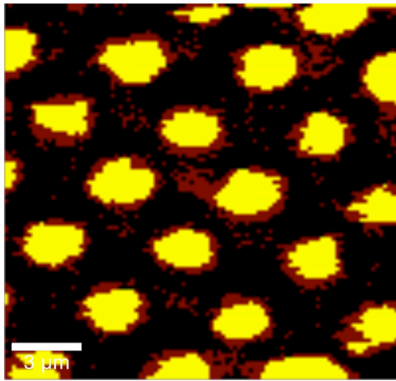


*Figure 3-2: Confocal Raman mapping image of sample grown on Si(111) <sup>[40]</sup>*

Cadmium telluride crystals have been observed in both zinc-blende phase and rock-salt phase. It is known that this material exhibits a phase transition from zinc-blende to rock-salt under increasing pressure <sup>[33, 34]</sup>. We also know that first order LO Raman scattering is allowed by symmetry in zinc-blende phase but it is not present in rock-salt phase. We therefore assign the 2LO Raman scattering to rock-salt phase. We investigate through confocal Raman the existence of the co-existence of the two phases. We use Cluster Analysis K-Means software and appropriate filter on the Raman system to detect both rock-salt and zinc-blende phases as according to their corresponding phonons. The LO band present in zinc-blende is centered around  $170\text{ cm}^{-1}$  while the 2LO band in rock-salt is centered around  $329\text{ cm}^{-1}$ . In all Raman image, we have assigned a brown color to LO phonons corresponding to zinc-blende phase and yellow color to 2LO phonons corresponding to rock-salt phase. In Fig 3-2 we can see mostly yellow, which is indicative of rock-salt under expected induced stress. Surrounding that, we observe unstrained zinc-blende CdTe. Because the crystals are partially located outside of the Si pillars in the  $2\text{ }\mu\text{m}$  separation in between, we conclude that this partial release of stress between zinc-blende and the Si pillar and the existence of the unstrained phase are due to the grain relaxation effect at its boundary.

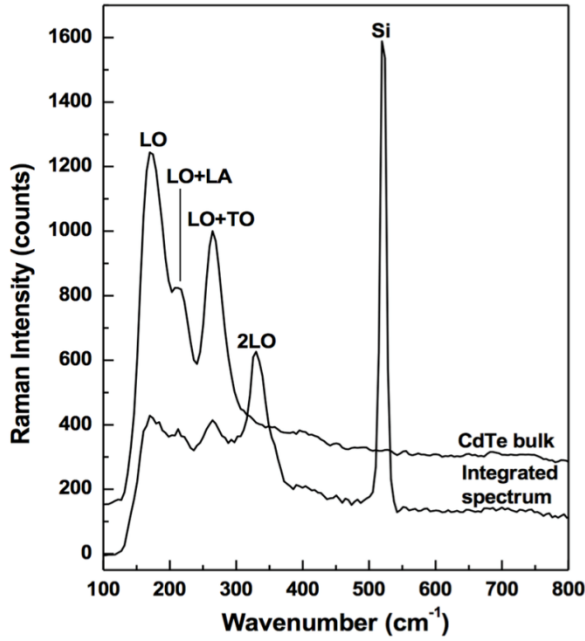


Figure 3-3: Raman spectra of bulk and a sample grown on silicon<sup>[40]</sup>

The integrated Raman spectrum of the sample grown on Si(111) and of the bulk CdTe are presented in Figs 3-3. The Raman spectrum for the bulk CdTe shows vibrations attributed to LO at  $148 \text{ cm}^{-1}$ , LO+LA at  $214 \text{ cm}^{-1}$ , and LO+TO at  $267 \text{ cm}^{-1}$ . If we take a closer look at the spectrum for the CdTe crystal grown on Si, we see the most prominent vibration at  $329 \text{ cm}^{-1}$ , which we attribute to the 2LO band of rock-salt and the less pronounced LO band of zinc-blende. These observations of the Raman spectrum are in good agreement with the visual observation of the Raman mapping image that shows a greater presence of the yellow representing rock-salt than the brown representing zinc-blende. We also note that low intensity of the LO band in comparison of the higher intensity of the 2LO indicates that the unstrained zinc-blende is less abundant than the rock-salt phase. We compare the position of the LO band

centered around  $170\text{ cm}^{-1}$  to the reported value of  $148\text{ cm}^{-1}$  in the literature. This large Raman shift can be attributed to strong spatial confinement of phonons in low-dimensional CdTe.

### 3.3 Raman analysis of sample grown on Si(211)

Similar to the Raman image of the sample grown on Si(111), the sample grown on Si(211) shows both strained and unstrained phases within the crystals with a stronger presence of the unstrained rock-salt phase as shown by Fig 3-4a-b. However, the average crystal size in this sample is larger than the former. Because of the difference of orientation of the silicon, we may attribute the size of the crystals to the orientation of the substrate. However, we must also consider that these Raman images are rather small areas in comparison to the size of the entire sample and it could be that the comparison of crystal sizes according to orientation of the substrate are a mere coincidence. Further tests are needed to support such a hypothesis.

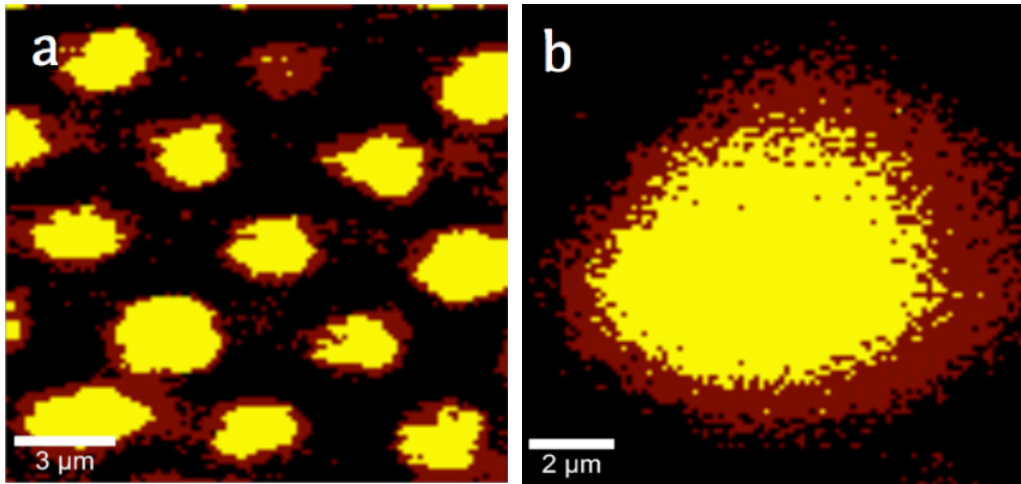


Figure 3-4: a) Confocal Raman mapping image of sample grown on Si(211) b) Confocal Raman mapping image of single crystal grown on Si(211)<sup>[40]</sup>

Fig 3-4b shows an uneven thickness of the unstrained phase at the crystal boundary and an elongation of the strained phase, from which we may conclude that Si(211) is a preferential

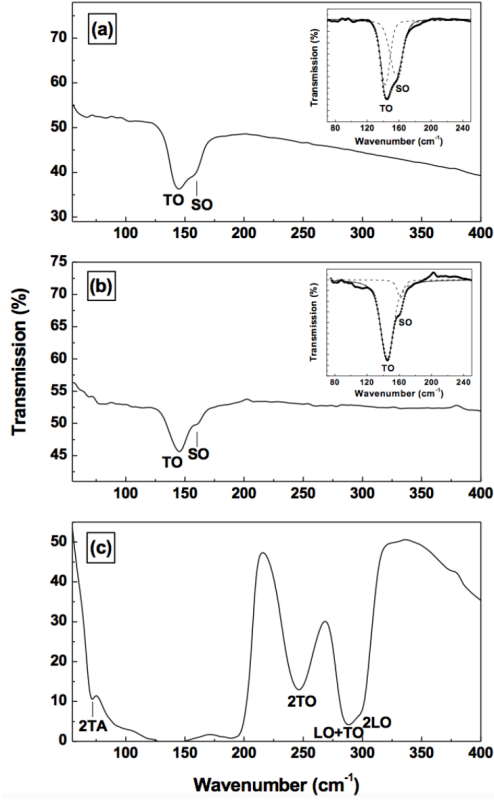
direction for the release of stress. Because of the nature of the growth process, crystals will favor growth in the direction of less induced strain. By giving the crystals more favorable growth conditions including a direction with less induced stress and adjustment to the Si pillar shape and size, we can optimize crystal growth for a better fabrication process.

We compare Figs 3-2 and 3-4, whose growth procedures were similar to one another, and conclude that the Raman image shown in Fig 3-4 (ie sample grown on Si(211)) exhibits more strain within the crystals in comparison to the Raman image in Fig 3-2. This increased stress can lead to non-uniform growth and the possibility of fused crystals. Fig 4b shows an extreme example of a fused crystal, which is approximately 8 microns in diameter. In analyzing the shape of the crystal, we deduce that three silicon pillars are supporting it. The center of the crystal shows an intense yellow color for the strained phase in the Raman mapping surrounded by uneven brown color representing the unstrained phase, which further strengthens our hypothesis for preferential release of stress of growth in this direction.

### 3.4 FTIR spectroscopy results

The infrared spectroscopy results are based on the absorption and transmission of infrared light by the sample. Figs 3-5a and 3-5b respectively show the FTIR spectra of the samples containing CdTe grown on Si(111) and on Si(211). Fig 3-5c shows the spectra given by the bulk CdTe that was used to grow these samples. This provides a baseline from which to compare for the samples. In Figs 3-5a and 3-5b we observe the TO band centered around  $139\text{ cm}^{-1}$  and the LO band centered around  $148\text{ cm}^{-1}$ ; between this is the phononic band gap in which the sample is completely opaque. In Fig 3-5c we observe the bulk expressing the following bands: 2TA centered around  $72\text{ cm}^{-1}$ , 2TO centered around  $250\text{ cm}^{-1}$ , LO+TO centered

around  $290\text{ cm}^{-1}$ , and 2LO centered around  $300\text{ cm}^{-1}$ . The 2LO band is of particular interest because it is located on the LO+TO shoulder whereas the others are free standing. Weaker, broader bands are present at  $97\text{ cm}^{-1}$  and  $188\text{ cm}^{-1}$ , which we attribute to LA and LO+TA respectively.



Figures 3-5: a) FTIR spectrum of sample grown on Si(111) b) FTIR spectrum of sample grown on Si(211) c) FTIR spectrum of bulk CdTe used for sample preparation<sup>[40]</sup>

In Figs 3-5a and 3-5b, we observe a TO band at  $143\pm 2\text{ cm}^{-1}$  with a weaker absorption maximum appearing as a shoulder on the higher-frequency end. The insets appearing in Figs 3-5a and 3-5b represent the fitting with Lorentzian lines on the spectra in this area of interest from about  $80\text{ cm}^{-1}$  to about  $240\text{ cm}^{-1}$ . We observe a broadening and shifting of the TO band



that agrees with the literature for the results for micro- and nano-crystals of CdTe <sup>[35-38]</sup>. The shoulder appearing on the TO band is attributed to SO phonons. Because the SO phonon mode is not allowed in bulk material, its presence indicate strong confinement in the samples. Eq 3-1 below shows the theoretical calculation of the frequency of SO phonons:

$$\omega_{SO}^2 = \omega_{TO}^2 \frac{\varepsilon_0 l + \varepsilon_m \times (l + 1)}{\varepsilon_\infty l + \varepsilon_m \times (l + 1)}$$

where  $\omega_{SO}$  is the frequency of SO mode,  $\omega_{TO}$  is the frequency of TO mode,  $\varepsilon_0$  is the static dielectric constant of CdTe,  $\varepsilon_\infty$  is the high-frequency dielectric constant of CdTe,  $\varepsilon_m$  is the dielectric constant of the matrix, and  $l$  is the angular momentum. In these experiments,  $\varepsilon_m = 1$ , odd values of  $l$  are IR active with  $l = 1$  being the most prominent, and even values of  $l$  are Raman active.

When we use a TO frequency of  $143 \text{ cm}^{-1}$  as we have measures, a static dielectric constant of 10.2 and a high-frequency dielectric constant of  $7.1^{[39]}$ , we obtain an SO mode frequency of  $165 \pm 2 \text{ cm}^{-1}$ . According to the IR spectra that belong to our samples, the SO frequency is centered around  $161 \pm 2 \text{ cm}^{-1}$ , which is in good agreement with the aforementioned theoretical value. From this information, we determine that SO confined phonons emerge from a complex mixture of TO mode and LO mode. Despite the theoretical calculation using the measured value of TO mode and minimizing inconsistency between experimental and theoretical values of SO phonon mode, the complexity of the confinement phenomenon is still not fully understood. We must note that a decrease in average size of crystals leads to an increase in absorption due to SO phonons in comparison to the absorption due to TO phonons. Comparing the IR spectra of the sample grown on Si(111) and Si(211) as shown on Figs 3-5a and 3-5b respectively, we note a more dominant presence of SO phonons in the sample grown on

Si(111). From that, we can conclude that on average, the crystals on Si(111) are smaller than the crystals on Si(211) similar to what we had determined from the Raman results.

## Chapter 4: Conclusions

The focus of this work was based on the characterization of CdTe grown on Si(211) and Si(111) by close-space sublimation using microscopic and spectroscopic techniques. Scanning electron microscopy, confocal Raman microscopy, Fourier-transform infrared absorption and Raman spectroscopies- were used to determine the uniformity, size, shape, crystallinity, and stoichiometry of the samples grown. The focus of this thesis is on FTIR and Raman spectroscopies. FTIR is based on the absorption and transmission of infrared light to determine the morphology of the sample. Confocal Raman microscopy uses the scattering of photons through collisions with the sample to map a selected area and obtain Raman spectra for individual points on the sample. These two complementary techniques allowed us to analyze the samples and individual crystals to determine their spectroscopic properties. Furthermore, confocal Raman spectroscopy was used to determine the release of stress and the preferential direction of growth for the crystals.

The different phonons describe different types of vibrations of the atoms within the sample. Because different phases are different on the molecular level, we can differentiate between them based on what is exhibited in the Raman spectrum. Existing literature states that CdTe has two possible lattice structures (rock-salt phase and zinc-blende phase) determined by different dominant phonon modes (2LO and LO respectively) consistent with phonon group theory. We determined rock-salt phase to be the strained phase and zinc-blende phase to be the unstrained phase. The morphology obtained through Raman mapping allowed us to analyze the shape and distribution of each of the phases leading us to the conclusion that the grain relaxation effect is responsible for the release of induced stress and the coexistence of the two

phases within a crystal. Through the comparison of the Raman mapping of the two samples in observing the uneven thickness of the unstrained phase we determined the preferential direction for release of stress.

Due to the size of the samples, another property we explored was the phonon confinement for each sample. Phonon confinement can be determined by the presence of surface mode (SO) phonons in small crystals, which we detected through FTIR spectra as a shoulder on the TO band. SO phonon presence increases with increasing surface area to volume ratio of the crystals. Because the frequency of SO phonons are purely theoretically calculated based on the nature of where they are found, we have calculated the assigned frequency value, which is in good agreement with the measured value. We are also able to measure in the samples all other phonon frequencies corresponding to, values characteristics to the bulk material through both FTIR and Raman.

In conclusion, FTIR was used to determine the crystallinity of the sample overall and to analyze phonon confinement; Raman was used to map small areas and individual crystals as well as to determine the stresses present in the crystals. Scanning electron microscopy and optical microscopy were used supplementally for imaging purposes. The crystals grown for this work have a future in solar cells and infrared detectors, but CdTe also has applications in radiation detection due to its atomic number and bandgap.

## References

- [1] D Bonnet, P Meyers, Cadmium-telluride—Material for thin film solar cells, Journal of Materials Research, Vol 13, No 10, pp 2740-2753, 1998
- [2] <http://www.physics.org/article-questions.asp?id=51>
- [3] <http://science.nasa.gov/science-news/science-at-nasa/2002/solarcells/>
- [4] PV Meyers, Design of a thin film CdTe solar cell, Solar Cells, Vol 23, Issues 1-2, pp 59-67, 1988
- [5] K Biswas, M Du, What causes high resistivity in CdTe?, Materials Science & Technology Division and Center for Radiation Detection Materials
- [6] A Rogalski, Infrared detectors: status and trends, Progression in Quantum Electronics Vol 27, pp 59-210, 2003
- [7] P Norton, HgCdTe infrared detectors, Opto-Electronics Review, Vol 10, No 3, pp 159-174, 2002
- [8] A Rogalski, Recent progress in infrared detector technologies, Infrared Physics and Technology, Vol 54, pp 136-154, 2011
- [9] JT Bushberg, TA Seibert, EM Leidholt Jr, JM Boone, The Essential Physics of Medical Imaging, Lippincott Williams & Wilkins, 2011
- [10] DS McGregor, H Hermon, Room-temperature compound semiconductor radiation detectors, Nuclear Instruments and Methods in Physics Research Section A: Accelerators, Spectrometers, Detectors, and Associates Equipment, Vol 395, Issue 1, pp 101-124, 1997
- [11] AV Rybka, LN Davydov, IN Shlyakhov, VE Kutny, IM Prokhoretz, DV Kutny, AN Orobinsky, Gamma-radiation dosimetry with semiconductor CdTe and CdZnTe detectors, Nuclear

Instruments and Methods in Physics Research Section A: Accelerators, Spectrometers, Detectors, and Associated Equipment, Vol 531, Issues 1-2, pp 146-156, 2004

[12] E Di Castro, R Pani, R Pellegrini, C Bacci, The use of cadmium telluride detectors for the qualitative analysis of diagnostic x-ray spectra, Physics in Medicine and Biology, Vol 29, No 9, pp 1117-1131, 1984

[13] C Scheiber, GC Giakos, Medical applications of CdTe and CdZnTe detectors, Nuclear Instruments and Methods in Physics Research Section A: Accelerators, Spectrometers, Detectors, and Associated Equipment, Vol 458, Issues 1-2, pp 12-25, 2001

[14] C Scheiber, New developments in clinical applications of CdTe and CdZnTe detectors, Nuclear Instruments and Methods in Physics Research Section A: Accelerators, Spectrometers, Detectors, and Associated Equipment, Vol 380, Issues 1-2, pp 385-391, 1996

[15] C Scheiber, B Eclancher, J Chambron, V Prat, A Kazandjan, A Jahnke, R Matz, S Thomas, S Warren, M Hage-Hali, R Regal, P Siffert, M Karman, Heart imaging by cadmium telluride gamma camera: European Program "BIOMED" consortium, Nuclear Instruments and Methods in Physics Research Section A: Accelerators, Spectrometers, Detectors, and Associated Equipment, Vol 428, Issue 1, pp 138-149, 1999

[16] Y Arntz, J Chambron, B Dumitresco, B Eclancher, V Prat, A portable cadmium telluride multidetector probe for cardiac function monitoring, Nuclear Instruments and Methods in Physics Research Section A: Accelerators, Spectrometers, Detectors, and Associated Equipment, Vol 428, Issue 1, pp 150-157, 1999

[17] R Triboulet, Y Marfaing, A Cornet, P Siffert, Undoped high resistivity cadmium telluride for nuclear radiation detectors, Journal of Applied Physics, Vol 45, Issue 6, pp 2759-2765, 1974

- [18] <http://www.lef.org/protocols/health-concerns/heavy-metal-detoxification/page-01>
- [19] K Zweibel, Impact of Tellurium Supply on Cadmium Telluride Photovoltaics, SCIENCE, Vol 328, pp. 699-701, 2012
- [20] VM Fthenakis, W Wang, Extraction and Separation of CdTe from cadmium Telluride Photovoltaic Manufacturing Scrap, Progress in Photovoltaics: Research and Applications, Vo 14, pp 363-371, 2006
- [21] [http://www.nobelprize.org/nobel\\_prizes/physics/laureates/1930/](http://www.nobelprize.org/nobel_prizes/physics/laureates/1930/)
- [22] <http://epsc.wustl.edu/haskin-group/Raman/faqs.htm>
- [23] LA Pinales, RR Chianelli, WG Durrer, R Pal, M Narayan, and FS Manciu: Spectroscopic study of inhibition of calcium oxalate calculi growth by Larrea Tridentata, Journal of Raman Spectroscopy, Vol 42, Issue 2, pp 259-264, 2011
- [24] [https://www.princeton.edu/~achaney/tmve/wiki100k/docs/Rayleigh\\_scattering.html](https://www.princeton.edu/~achaney/tmve/wiki100k/docs/Rayleigh_scattering.html)
- [25] P Dacha thesis Inhibition Of Calcium Oxalate Calculi By Ndga – A Spectroscopic Study
- [26] <http://www.andor.com/learning-academy/raman-spectroscopy-an-introduction-to-raman-spectroscopy>
- [27] [http://rdrs.uaic.ro/raman\\_spectroscopy/2010/04/quantum-and-classical-raman-theory/](http://rdrs.uaic.ro/raman_spectroscopy/2010/04/quantum-and-classical-raman-theory/)
- [28] The Infracord double-f, Clinical Science, Vo 16, No 2, 1957
- [29] [http://www.phy.davidson.edu/stuhome/cabell\\_f/diffractionfinal/pages/michelson.htm#History](http://www.phy.davidson.edu/stuhome/cabell_f/diffractionfinal/pages/michelson.htm#History)
- [30] <http://www.muelaner.com/wp-content/uploads/2013/07/Interferometer.jpg>
- [31] <http://pharmaxchange.info/press/2012/04/ultraviolet-visible-uv-vis-spectroscopy-%E2%80%93-derivation-of-beer-lambert-law/>

- [32] EJ Danielewicz, PD Coleman, Far Infrared Optical Properties of Selenium and Cadmium Telluride, Applied Optics, Vol 13, No 5, pp 1164-1170, 1974
- [33] A Onodera, High pressure transition in cadmium telluride, Rev. Phys. Chem Japan, Vol 9, No 2, pp 78-92, 1968
- [34] PTC Freire, MAA Silva VCS Reynoso, AR Vaz, V Lemos, Pressure Raman scattering of CdTe quantum dots, Phys Rev B, Vol 55, No 11, pp 6743-6746, 1997
- [35] R Ruppini, R Englman, Optical phonons of small crystals, Rep Prog Phys, Vol 33, pp 149-196, 1970
- [36] E Roca, C Trallero-Giner, M Cardona, Polar optical vibrational modes in quantum dots, Phys Rev B, Vol 49, No 19, pp 13704-13611, 1994
- [37] MC Klein, F Hache, D Richard, C Richard, C Flytzanis, Size dependence of electron-phonon coupling in semiconductor nanosphere: The case of CdSe, Phys Rev B, Vol 42, pp 11123-11132, 1990
- [38] V Dzhan, I Lokteva, C Himcinschi, X Jim, J Kolny-Olesiak, DRT Zahn, Phonon raman spectra of colloidal CdTe nanocrystals: effects of size, non-stoichiometry and ligand exchange, Nanoscale Res Lett, Vol 6, No 79, pp 1-10, 2011
- [39] JM Rowe, RM Nicklow, DL Price, K Zano, Lattice dynamics of cadmium telluride, Phys Rev V, Vol 10, pp 671-675, 1974
- [40] Felicia S. Manciu, Ph.D.; Jessica G Salazar; Aryzbe Diaz; Stella A Quinones, Ph.D.  
Spectroscopic, microscopic, and internal stress analysis in cadmium telluride grown by close-space sublimation



## Curriculum vita

Jessica G Salazar was born in El Paso, Texas as the second daughter of Luis and Yolanda Salazar and only sister to Jennifer Munoz. She graduated from JM Hanks High School in 2009 and continued her studies at the University of Texas at El Paso where she finished her Bachelor of Science in Physics degree in 2013 and continued onto a Master of Science in Physics degree, which she completed in 2013. During her studies, Jessica worked as a tutor, peer leader, teaching assistant, and research assistant at JM Hanks High School, UTEP Chemistry department, UTEP Physics department, and UTEP Physics department respectively. Jessica is continuing her studies by pursuing a Doctorate in Medical Physics at Vanderbilt University in Nashville, Tennessee. During her Master's studies, she coauthored *A Drude model analysis of conductivity and free carriers in boron-doped diamond films and investigations of their internal stress and strain* published in Journals of Materials Science as well as *Spectroscopic, microscopic, and internal stress analysis in cadmium telluride grown by close-space sublimation* in Thin Solid Films. In addition to that, immediately after her graduation from her Bachelor's degree, Jessica was a coauthor and sole editor of *Peer-Led Team Learning Resource Book: Second Semester General Chemistry* that was used in Second-semester General Chemistry at UTEP.

Permanent address:

3300 Itasca St

El Paso, TX 79936